

See discussions, stats, and author profiles for this publication at: <https://www.researchgate.net/publication/231645581>

Hydrothermal Synthesis, Cubic Structure, and Luminescence Properties of BaYF₅:RE (RE = Eu, Ce, Tb) Nanocrystals

ARTICLE *in* THE JOURNAL OF PHYSICAL CHEMISTRY C · OCTOBER 2010

Impact Factor: 4.77 · DOI: 10.1021/jp105061x

CITATIONS

57

READS

38

8 AUTHORS, INCLUDING:



Hongpeng You

Chinese Academy of Sciences

178 PUBLICATIONS 3,414 CITATIONS

SEE PROFILE



Yanhua Song

Jilin University

88 PUBLICATIONS 1,842 CITATIONS

SEE PROFILE



Ning Guo

University of Shanghai for Science and Tec...

66 PUBLICATIONS 1,475 CITATIONS

SEE PROFILE

Hydrothermal Synthesis, Cubic Structure, and Luminescence Properties of BaYF₅:RE (RE = Eu, Ce, Tb) Nanocrystals

Yeju Huang,^{†,‡} Hongpeng You,^{*,†} Guang Jia,^{†,‡} Yanhua Song,^{†,‡} Yuhua Zheng,^{†,‡} Mei Yang,^{†,‡} Kai Liu,^{†,‡} and Ning Guo^{†,‡}

State Key Laboratory of Rare Earth Resource Utilization, Changchun Institute of Applied Chemistry, Chinese Academy of Sciences, Changchun 130022, People's Republic of China, and Graduate University of the Chinese Academy of Sciences, Beijing 100049, People's Republic of China

Received: June 2, 2010; Revised Manuscript Received: September 10, 2010

BaYF₅ nanocrystals with a mean size of about 24 nm have been prepared via a facile hydrothermal method without the assistance of any surfactant for the first time. The structure investigation reveals that the as-synthesized BaYF₅ nanocrystals are cubic structures instead of the reported tetragonal structures found via a Rietveld refinement method with GSAS, a Rietveld refinement package. The XRD and SEM analyses demonstrate that the size and morphology of the products are insensitive to the variation of experimental conditions. The photoluminescence properties of the Eu³⁺, Ce³⁺, and Tb³⁺ single-doped as well as Ce³⁺-Tb³⁺ codoped BaYF₅ nanocrystals were characterized. The results reveal that the existence of the Ce³⁺ ions can dramatically enhance the emission intensity of the Tb³⁺ ions, due to an efficient energy transfer from the Ce³⁺ to Tb³⁺ ions in the BaYF₅:Ce³⁺,Tb³⁺ nanocrystals. The critical energy transfer distance between the Ce³⁺ and Tb³⁺ ions was calculated by methods of concentration quenching and spectral overlapping. Analysis and calculation reveal that the dipole–quadrupole interaction should be mainly responsible for the energy transfer and the accurate oscillator strength ratio of the electric quadrupole to dipole transitions for the Tb³⁺ ion is about 10^{−3}.

1. Introduction

Over the past decades, the study of nanometric luminescent materials, especially lanthanide ion-doped luminescent nanomaterials, has become one of the hottest topics in nanoscience because of their great potential applications in light-emitting devices, low-threshold lasers, optical amplifiers, and biological labels.^{1–3} In nanoscale materials, it is acknowledged that many factors, such as the degree of crystallinity, size, morphology, surface state, and impurities, have significant effects on the physical, chemical, and electronic properties of the nanoparticles.^{4–6} In recent years, material scientists have explored various synthetic strategies, including physical,⁷ chemical,⁸ and biosynthetic methods,⁹ for syntheses of reproducible and controllable nanocrystals with uniform size, morphology, and chemical composition. As the intrinsic growth natures, particles with larger size are usually more easily generated in water solution than in organic solutions. Furthermore, in order to control the growth of nanoparticles, organic surfactants or capping ligands have been frequently introduced. To date, fluoride nanocrystals with small sizes have been predominantly prepared via high-temperature thermal decomposition methods in organic solvents under inert atmosphere protection. Nevertheless, the toxicity of the solvents, ligands, and precursors, along with the luminescence quenching effect of these organic materials used might limit the applications of these nanoparticles to a certain extent.

Therefore, it is desirable to synthesize nanometric luminescent materials with small sizes in water solution without any organic reagents.

Metal fluorides have a number of uncommon properties, for example, low phonon energy, electron-acceptor behavior, a large optical-transmission domain, high resistivity, and anionic conductivity. Owing to their potential applications in displaying, lasing, and biolabeling, various kinds of metal fluorides in nano-/microscale size were intensively researched in recent years.^{10–13} For example, in our previous work, we have reported the syntheses of the Eu-doped Ba_{0.92}Y_{2.15}F_{8.29} submicrospheres via a hydrothermal method for the first time.¹⁴ Compared with other fluorides, tetragonal BaYF₅ bulk crystal is considered to be an excellent host matrix for downconversion and upconversion luminescence.^{15,16} However, there is only little literature available on the generation of hydrophobic BaYF₅ nanocrystals, which are ascribed to tetragonal structure.^{17,18} Studies about hydrothermal synthesis of cubic structure BaYF₅ nanocrystals without any surfactant assistance have not yet been reported. Moreover, energy transfer from Ce³⁺ (sensitizer) to Tb³⁺ (activator) has been observed and investigated in many phosphors, such as Ca₃Y₂(Si₃O₉)₂:Ce³⁺,Tb³⁺,¹⁹ GdMgB₅O₁₀:Ce,Tb,²⁰ LaMgAl₁₁O₁₉:Ce,Tb,²¹ and Al₂O₃–B₂O₃:Ce,Tb.²² But no study has reported on the Ce³⁺–Tb³⁺ energy transfer in cubic BaYF₅ nano/microcrystals up to now.

Herein, we presented a synthesis of BaYF₅ nanocrystals with a mean size of about 24 nm via a facile and inexpensive hydrothermal route without using any organic solvent or surfactant for the first time. Different from the reported literature, we figured out that the as-synthesized BaYF₅ nanocrystals are cubic structure instead of tetragonal by a Rietveld refinement method with GSAS, a Rietveld refinement package.^{23,24} A series of control experiments were carried out to investigate the

* To whom correspondence should be addressed. Tel.: +86-431-85262798. Fax: +86-431-85698041. E-mail: hpyou@ciac.jl.cn.

[†] Changchun Institute of Applied Chemistry, Chinese Academy of Sciences.

[‡] Graduate University of the Chinese Academy of Sciences.

influences of experimental conditions on the size and morphology of BaYF₅ nanocrystals. The photoluminescence properties of the Eu³⁺, Ce³⁺, and Tb³⁺ single-doped as well as Ce³⁺–Tb³⁺ codoped BaYF₅ nanoparticles were characterized. Moreover, the energy transfer efficiency (η_T), the Ce³⁺–Tb³⁺ critical distance (R_c), and the mechanism of the energy transfer from the Ce³⁺ to Tb³⁺ ions in the BaYF₅:Ce³⁺,Tb³⁺ nanocrystals have been discussed in detail. Our results indicate that the cubic structure BaYF₅ nanocrystals are also an excellent host matrix for doping lanthanide ions.

2. Experimental Section

2.1. Sample Preparation. Lanthanide nitrate solutions were obtained by dissolving lanthanide oxide (99.99%) in dilute nitric acid solution under heating with agitation. All the other chemicals were of analytical grade and used as received without further treatment.

In a typical procedure of preparing BaYF₅ nanocrystals, 1 mmol of BaCl₂·2H₂O and 1 mL of 1 mmol/L Y(NO₃)₃ were first added into 15 mL of deionized water with stirring to form a transparent solution. Subsequently, 15 mL of aqueous solution containing 5.40 mmol of NH₄F (0.20 g) was added into the above solution. After the addition of the NH₄F, the transparent solution became white turbid. After stirring for about 30 min, the resultant solution was transferred into a 50 mL Teflon autoclave, and additional deionized water was added into the autoclave until about 80% of its volume. Finally, the autoclave was sealed and heated at 180 °C for 24 h followed by cooling to room temperature naturally. The resulting precipitates were washed with deionized water and ethanol each two times. The final product was dried at 60 °C in air. For the preparation of lanthanide doped BaYF₅ nanocrystals, the corresponding amounts of lanthanide nitrate solutions were added to replace Y(NO₃)₃ at the initial stage.

In preparation BaYF₅ nanocrystals by using ethylenediaminetetraacetic acid (EDTA) as a chelator, a certain amount of EDTA was first added into 15 mL of deionized water. Under magnetic stirring, ammonia (25 wt %) solution was added dropwise until EDTA was totally dissolved to form a transparent solution with a pH value of ~9. Then 1 mmol of BaCl₂·2H₂O and 1 mL of 1 mmol/L Y(NO₃)₃ were added into the above transparent solution. The subsequent operations were identical to the typical preparation of BaYF₅ nanocrystals without EDTA as a chelator.

2.2. Characterization. Powder X-ray diffraction data of all the products were collected on a Bruker D8 focus X-ray powder diffractometer using Cu K α radiation operating from $2\theta = 15^\circ$ to 85° , with a step size of 0.02° . The powder X-ray diffraction data for Rietveld refinement of the structure was subjected to GSAS, which is capable of handling and refining the step analysis diffraction data in a comprehensive manner. The size, morphology, and composition of the products were characterized using a Hitachi S-4800 field emission scanning electron microscope (FE-SEM) equipped with an energy dispersive X-ray (EDX) spectrometer, operated at an acceleration voltage of 10 kV. The transmission electron microscope (TEM) and selected area electron diffraction (SAED) patterns were obtained by a FEI Tecnai G2 transmission electron microscope at the accelerating voltage of 200 kV. Photoluminescence (PL) emission and excitation spectra of the products were recorded with a Hitachi F-4500 fluorescence spectrophotometer equipped with a 150 W xenon lamp as the excitation source with the same instrument parameters. The emission decay curves were obtained from a Lecroy Wave Runner 6100 digital oscilloscope (1 GHz) using a tunable laser (pulse width = 4 ns, gate = 50 ns) as the

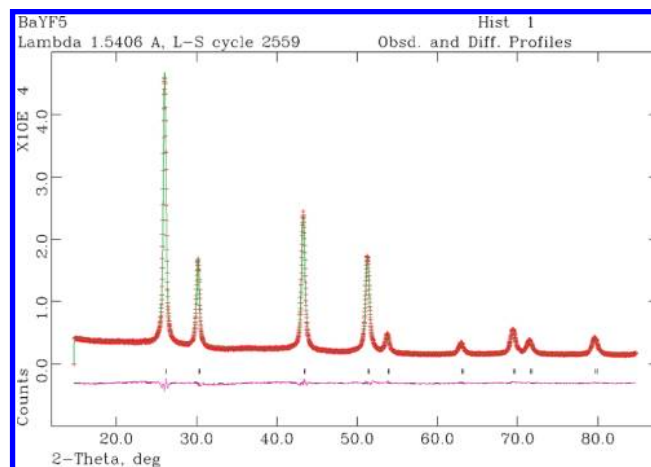


Figure 1. Rietveld refinement pattern of the as-synthesized BaYF₅ nanocrystals. The “+” are the raw X-ray diffraction data and the overlapping continuous line is the calculated pattern. Black vertical lines in the profile indicate the Bragg’s positions of the allowed reflections for Cu K α_1 and K α_2 . The curve at the bottom is the difference in the observed and calculated intensities in the same scale.

excitation source (Continuum Sunlite OPO). All the measurements were performed at room temperature.

3. Results and Discussion

3.1. Crystal Structure, Morphology, and Growth Process of the Nanocrystals. The powder XRD data of the as-synthesized product shows nine characteristic diffraction peaks (26.22° , 30.37° , 43.49° , 51.45° , 53.95° , 63.15° , 69.60° , 71.72° , 79.76°) in 2θ range of 15° to 85° . Compared with the tetragonal structure BaYF₅ (JCPDS 46–0039, space group P-421 m, $z = 10$, cell parameters $a = 12.468$ Å, $c = 6.78$ Å), the absence of some diffraction peaks implies that the crystal structure of the as-synthesized product may have a higher symmetry in space group. In contrast, all of these peaks are coincident with the cubic structure BaCeF₅ (JCPDS 43–0394, space group $Fm\bar{3}m$, $Z = 2$) except slight shifting toward higher 2θ side. And taking consideration of the contraction of the cell parameter induced by the smaller radius of Y³⁺ ions, we assume that the as-synthesized product belongs to a face-centered cubic structure instead of the reported tetragonal structure. To support this assumption, we take the structure of BaCeF₅ (JCPDS 43–0394) as the model for Rietveld refinement. The Rietveld refinement of the powder XRD data was performed by the least-squares method using GSAS software. The observed and calculated plots of the Rietveld refinement, as well as that showing the difference between them, are reported by Figure 1. A rather good agreement and acceptable reliability factors: $R_{wp} = 3.81\%$, $R_p = 2.93\%$, $R_2 = 3.78\%$ have been found. Details of the crystal structure and the equivalent isotropic parameters are given in Table 1. In the lattice of face-centered cubic structure BaYF₅, the Ba²⁺ and Y³⁺ ions occupy the same 4a Wyckoff position in half. The fluoride ions partially occupy four different Wyckoff positions of 4b, 8c, 32i, and 48f. To investigate the real composition of the as-synthesized product, energy-dispersive X-ray (EDX) spectrum analysis was carried out and the result is shown in Figure 2. It confirms the presence of elements Ba, Y and F in the product and the obtained atomic ratio of Ba/Y/F is 1: 1.008: 5.124, which is approaching the theoretical atomic Ba/Y/F ratio (1: 1: 5) in BaYF₅. It is worth noting that the diffraction peaks are widened as a result of the small-size effect of the nanocrystals. The mean crystallite size of the product

TABLE 1: Details of the Crystal Structure and Equivalent Isotropic Parameters

structure			cubic			
space group			f m $\bar{3}$ m			
lattice parameters			$a = b = c = 5.890 \text{ \AA}$, $\alpha = \beta = \gamma = 90^\circ$			
Z			2			
volume of unit cell			204.360 \AA^3			
unit cell formula weight			645.463			
density _{X-ray}			5.245 g/cm^{-3}			
atom	Wyckoff positions	x	y	z	occupancy	$U_{\text{iso}} (\text{\AA}^2)$
Ba1	4a	0	0	0	0.5	0.03397
Y2	4a	0	0	0	0.5	0.03397
F3	8c	0.25	0.25	0.25	0.765	0.06476
F4	48f	0.5	0.1225	0.1225	0.0433	0.00100
F5	32i	0.3676	0.3676	0.3676	0.0575	0.07518
F6	4b	0.5	0.5	0.5	0.03	0.07362

was estimated from the XRD pattern according to the Scherrer formula $D = K\lambda/(\beta\cos\theta)$, where λ is the X-ray wavelength (0.15406 nm), β is the full-width at half-maximum, θ is the diffraction angle, and K is a constant (0.89). The strongest diffraction peak at $2\theta = 26.22^\circ$ was used to calculate the mean crystalline size of the nanocrystals. The estimated mean crystallite size is 23.9 nm.

A representative panoramic SEM image shown in Figure 3a demonstrates that the product is composed of well dispersed particles with small sizes. The high-magnified TEM image (Figure 3b) further shows the nanocrystals more distinctly. Most of the nanocrystals are pseudospherical particles with a mean size of about 24 nm, which is in consistent with the size estimated by Scherrer formula from the XRD pattern, indicating that the as-obtained nanocrystals are essentially single crystalline in nature. The selected-area electron diffraction (SAED) in Figure 3c exhibits dot-rings, which are due to the diffraction of ensemble nanocrystals. The interplanar distances obtained from the first four dot-rings are 3.396, 2.943, 2.080, and 1.775 \AA , which can be assigned to 111, 200, 220, and 311 lattice planes of cubic structure BaYF₅, respectively.

In addition to the above undoped BaYF₅ nanocrystals, Eu³⁺, Ce³⁺, Tb³⁺ single-doped and Ce³⁺–Tb³⁺ codoped BaYF₅ nanocrystals were also prepared. As the doping of different lanthanide ions in BaYF₅ did not change the phase structure, crystallinity, and morphology of the products in our system (see Figure S1 in the Supporting Information), we mainly took the undoped BaYF₅ nanocrystals for example to investigate the

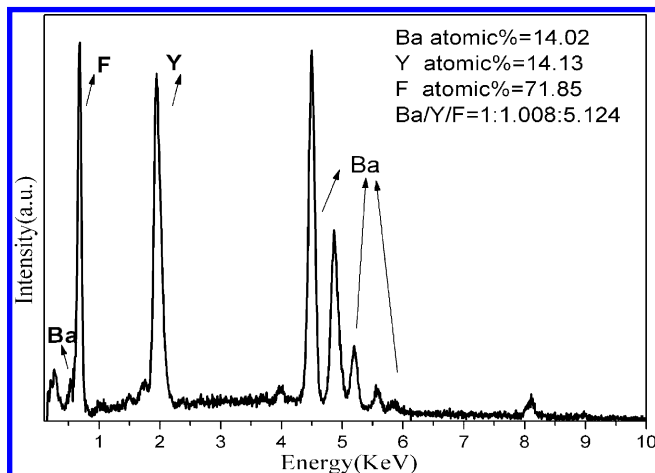
influences of experimental parameters on the phase structure, size, and morphology.

3.1.1. Effects of pH. The pH values of the solution were tuned by introducing nitric acid or ammonia. The XRD and SEM results reveal that the BaYF₅ nanocrystals with similar size and morphology can be obtained in a relative wide pH ranging from 2 to 10. If the pH value was adjusted to 1, the obtained sample consists of irregular orthorhombic YF₃ truncated octahedral microcrystals (see Figure S2 in the Supporting Information) since BaF₂ is soluble in strong acidic solution (pH = 1), while the influence of the pH variation on the solubility of YF₃ is faint.

3.1.2. Effects of EDTA. To investigate the influence of chelator EDTA, three samples (S3a, S3b, S3c) were produced by using 0.15 g, 0.30 g, and 0.60 g EDTA as a chelator as described in experimental section, respectively. In comparison with the BaYF₅ nanocrystals produced without EDTA as shown in Figure 3, size and morphology differences between the samples of S3a and S3b are faint, while the sample S3c was seriously agglomerated (see Figure S3 in the Supporting Information). It seems that appropriate amount of chelator EDTA has little influence on the growth of the BaYF₅ nanocrystals while the excess chelator EDTA would induce agglomeration of these nanocrystals. This situation is somewhat contrary to the general cases, where chelator or surfactant adsorbed on specific faces of crystals controls the growth rate of crystals as well as avoids nanocrystals agglomeration.²⁵

3.1.3. Effects of Barium Sources. To investigate the effects of barium sources, three different kinds of barium sources (BaCl₂, Ba(CH₃COO)₂, and Ba(NO₃)₂) were used in the experiments. The BaYF₅ nanocrystals produced with Ba(CH₃COO)₂ and Ba(NO₃)₂ as barium source both consists of nanoparticles with size and morphology similar to those produced with BaCl₂ (see Figure S4 in the Supporting Information). That is to say, the crystal growth was also insensitive to the anions in the solution.

In order to further shed light on the crystal growth process of the BaYF₅ nanocrystals, experiments with different hydrothermal treatment intervals (0 h, 1 h, 6 h, 12 h) were also carried out. It is found that all the XRD patterns of these samples are in agreement with the cubic structure BaYF₅ irrespective of the hydrothermal treatment intervals (see Figure S5 in the Supporting Information). Intensity of the diffraction peaks increases with the hydrothermal treatment time, implying the improvement of crystallinity. The mean crystalline size of these samples under different hydrothermal treatment intervals were 15.5 nm (1 h),

Figure 2. EDX spectrum of the as-synthesized BaYF₅ nanocrystals.

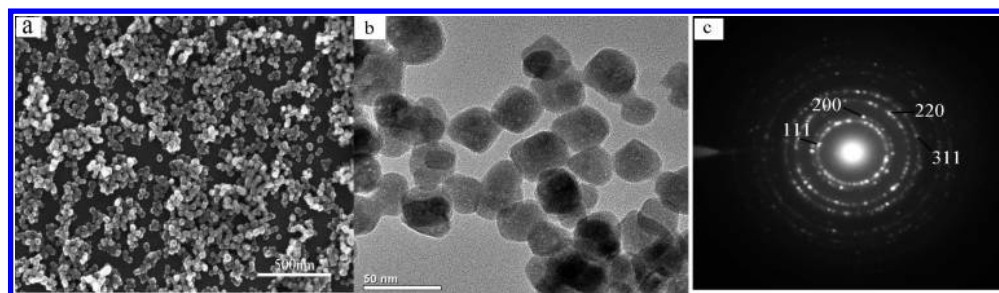


Figure 3. (a) SEM image, (b) TEM image, and (c) the SAED pattern of as-synthesized BaYF₅ nanocrystals.

18.2 nm (6 h), and 19.6 nm (12 h), which were estimated by Scherrer formula from the corresponding XRD patterns, respectively. It indicates that the increase of nanocrystal size with hydrothermal treatment time is slight. The SEM images were also used to examine the sizes and morphologies of these samples (see Figure S6 in the Supporting Information). The sample produced by direct coprecipitation of the salts without hydrothermal treatment (0 h) was badly crystallized nanoparticle clusters, which were agglomerated by very tiny particles and had rough surfaces. As the hydrothermal treatment time increased from 1 to 12 h, these particle clusters gradually disappeared and well dispersed nanocrystals appeared with a pseudospherical morphology while the increase of the particle size is small, which is coincident with the XRD results.

On the basis of the above results, we made a conjecture about the growth process of the BaYF₅ nanocrystals. First, the addition of F⁻ ions brought a high degree of supersaturation in the solution giving rise to the eruptible coprecipitation of the Ba²⁺ and Y³⁺ ions simultaneously, so many BaYF₅ nuclei were formed in a very short time. To minimize their surface energy, these BaYF₅ nuclei went through a quick agglomeration process resulting in the formation of nanoparticle clusters.^{26,27} With assistance of the hydrothermal treatment under high pressure and temperature, these badly crystallized nanoparticle clusters experienced a process of recrystallization and crystal growth. Since most of the target constituents (Ba²⁺, Ln³⁺, F⁻) were consumed at the fast nucleation stage, the further growth of BaYF₅ nanocrystals at the ripening process was difficult. It was presumed that the recrystallization and crystal growth of BaYF₅ nanoparticles were mainly through the dissolution of BaF₂ and the transferring of the corresponding Ba²⁺ and F⁻ ions in the BaYF₅ nanoparticles. As a result, the cubic structure was preserved and the increase of BaYF₅ nanoparticles size was slight.

With respected to the face-centered cubic structure BaYF₅ crystal, we must bear in mind that BaF₂ crystal is crystallized in the same *Fm* $\bar{3}$ *m* space group (fluorite structure) and has larger Lattice parameters $a = b = c = 6.2001$ Å. In viewpoint of the atom sites in the unit cell, the Y³⁺ cations substitute half of the Ba²⁺ cation sites at the same time F⁻ anions enter the interstitial sites for charge balance compensation. In the crystal lattice of BaF₂, the Ba²⁺ cations occupied highly symmetrical octahedral (*O_h*) cubic centers. In BaYF₅, Ba²⁺ and nonlocally charge compensated lanthanide cations would form octahedral (*O_h*) cubic centers. Alternatively, the charge compensated lanthanide cations by F⁻ interstitials in either nearest-neighbor or next-nearest-neighbor positions would form tetragonal (*C_{4v}*) or trigonal (*C_{3v}*) centers, respectively. Clustering of such defects readily occurs, resulting in a variety of possible cluster configurations.^{28,29} So in the lattice of BaYF₅, lanthanide cations occupied crystal sites with lower point symmetry (*C_{4v}*, *C_{3v}*), especially for the high lanthanide concentration doped BaYF₅

nanocrystals. The lower point symmetry of lanthanide ions in BaYF₅ may be one of the reasons for the high photoluminescence efficiency of the doped BaYF₅ nanocrystals, which will be shown in the later part of this work. The cubic unit cell of BaF₂ acted as structure model or structure director for the formation of cubic structure BaYF₅ nanocrystals. We supposed that there were two prerequisites for its structure model or structure director role. The first prerequisite was that the larger radius of Ba²⁺ in comparison with that of the Y³⁺ so that the Y³⁺ ions can easily enter the unit cell of BaF₂ for occupying the Ba²⁺ site. The second prerequisite was the proper solubility of BaF₂, which may be favorable for Ba²⁺ and F⁻ ions transferring to the energy-favor sites to keep the cubic structure unchanged.

3.2. PL Properties of the BaY_{0.95}Eu_{0.05}F₅ Nanocrystals.

Figure 4 gives the PL excitation ($\lambda_{\text{em}} = 590$ nm) and emission ($\lambda_{\text{ex}} = 396$ nm) spectra of the BaY_{0.95}Eu_{0.05}F₅ nanocrystals. The excitation spectrum consists of the characteristic excitation peaks of the Eu³⁺ ions corresponding to the direct excitation from the ground state to higher excited states of the Eu³⁺. The maximum excitation peak at 396 nm is attributed to the ⁷F₀ → ⁵L₆ transition of the Eu³⁺ ions. Excited into 396 nm, the emission spectrum of the BaY_{0.95}Eu_{0.05}F₅ nanocrystals shows several emission peaks in range from 500 to 700 nm, which are ascribed to the ⁵D₁ and ⁵D₀ to ⁷F_{*J*} (*J* = 0, 1, 2, 3, 4) transitions of the Eu³⁺ ions, respectively. The emission spectrum is dominated by the transition of the ⁵D₀ → ⁷F₁ transition (590 nm), which is a magnetic dipole transition and not affected much by crystal field around the Eu³⁺ ion.³⁰ Different from the ⁵D₀ → ⁷F₁ transition, the ⁵D₀ → ⁷F₂ transition located at 615 nm is an electrical dipole-allowed transition and hypersensitive to the local environment. In general, Eu³⁺ ions are usually employed as a sensitive probe to investigate the coordination and local environment around the cations substituted in the crystalline lattice based on the fact that the ⁵D₀ and ⁷F₀ levels are not subjected to crystal field splitting while the splittings of the emission or absorption transitions involving the ^{2s+1}L_{*J*} multiplets with *J* > 0 are symmetry-dependent. The intensity ratios of the ⁵D₀ → ⁷F₁ (590 nm) transition with that of the ⁵D₀ → ⁷F₂ (615 nm) transition can provides some structural information such as distortion of ligand environment and site symmetry.³¹ The ratio of the ⁵D₀ → ⁷F₁ (590 nm) to ⁵D₀ → ⁷F₂ (615 nm) transitions of the BaY_{0.95}Eu_{0.05}F₅ nanocrystals is about 5, indicating that the Eu³⁺ ions locate at the sites of inversion symmetry in the BaYF₅ host matrix and further proving the rationality of the face-centered cubic structure.

3.3. PL Properties of the BaY_{0.80}Ce_{0.20}F₅ and BaY_{0.80}Tb_{0.20}F₅ Nanocrystals. Figure 5a shows the PL excitation ($\lambda_{\text{em}} = 330$ nm) and emission ($\lambda_{\text{ex}} = 291$ nm) spectra of the BaY_{0.80}Ce_{0.20}F₅ nanocrystals. The excitation spectrum of the BaY_{0.80}Ce_{0.20}F₅ nanocrystals gives a broadband centered at 265 nm with a shoulder centered at 291 nm, which were attributed

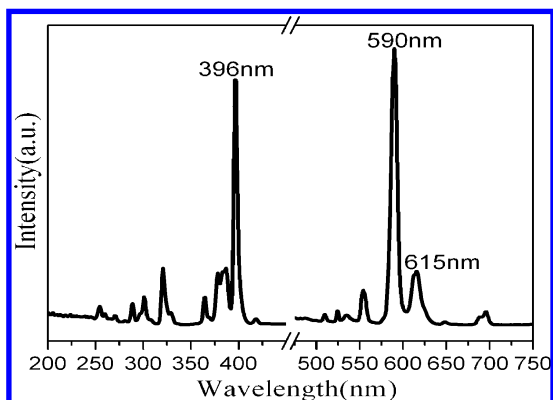


Figure 4. Excitation ($\lambda_{em} = 590$ nm) and emission ($\lambda_{ex} = 396$ nm) spectra of the BaY_{0.95}Eu_{0.05}F₅ nanocrystals.

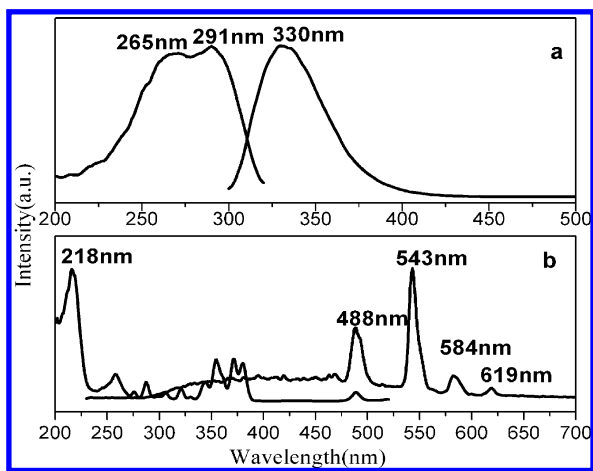


Figure 5. Excitation and emission spectra of (a) BaY_{0.80}Ce_{0.20}F₅ ($\lambda_{em} = 330$ nm, $\lambda_{ex} = 291$ nm), and (b) BaY_{0.80}Tb_{0.20}F₅ ($\lambda_{em} = 543$ nm, $\lambda_{ex} = 218$ nm).

to the electric dipole-allowed transitions of the Ce³⁺ ions from the 4f shell to the 5d orbital. Owing to the influences of crystal field splitting and spin–orbit coupling, the 4f \rightarrow 5d transition of the Ce³⁺ ions will exhibit a subtle structure. So the excitation spectrum of the Ce³⁺ ions shows the direct splitting information of 5d orbital in the crystal field.³² Under excitation at 291 nm, the emission spectrum of BaY_{0.80}Ce_{0.20}F₅ nanocrystals exhibits an intense ultraviolet emission band centered at 330 nm, which is assigned to the 5d-4f electronic transition of the Ce³⁺ ions.

Figure 5b gives the excitation ($\lambda_{em} = 543$ nm) and emission ($\lambda_{ex} = 218$ nm) spectra of the BaY_{0.80}Tb_{0.20}F₅ nanocrystals. The excitation spectrum exhibits two broadbands in the range from 200 to 270 nm and a number of narrow bands in the region from 270 to 500 nm. The strong broadband at about 218 nm is due to the spin-allowed 4f \rightarrow 5d transition of the Tb³⁺ ions. The weak broadband at about 258 nm is assigned to the spin-forbidden transition of the Tb³⁺ ions, while the narrow bands are attributed to absorption of the forbidden f-f transitions.^{33,34} The emission spectrum consists of four main peaks at 488, 543, 584, and 619 nm, which originate from the ⁵D₄ to ⁷F_J ($J = 6, 5, 4, 3$) transitions of the Tb³⁺ ions, respectively. Among these emission peaks, the green emission at 543 nm (⁵D₄ \rightarrow ⁷F₅) is the strongest one because it is a magnetic dipole allowed transition.³⁵

3.4. Energy Transfer in BaY_{0.80-x}Ce_{0.20}Tb_xF₅ Nanoparticles. On the basis of the above PL spectra of the Ce³⁺ and Tb³⁺ single-doped samples, one can find that the emission band of the Ce³⁺ ions well overlap with the excitation band of the Tb³⁺ ions. Therefore, it is expected that a resonance-type energy

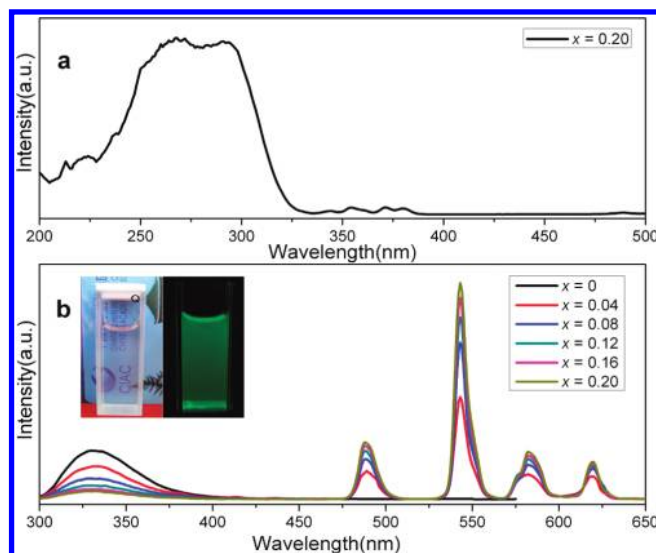


Figure 6. (a) Excitation spectrum of BaY_{0.60}Ce_{0.20}Tb_{0.20}F₅ nanocrystals ($\lambda_{em} = 543$ nm), (b) Emission spectra of the BaY_{0.80-x}Ce_{0.20}Tb_xF₅ nanocrystals with different Tb³⁺ concentrations ($\lambda_{ex} = 291$ nm) (Inset of b are the photographs of pellucid dispersion of BaY_{0.60}Ce_{0.20}Tb_{0.20}F₅ nanocrystals in deionized water under ambient and irradiation of a 254 nm UV lamp, respectively).

transfer from Ce³⁺ to Tb³⁺ in BaYF₅:Ce,Tb nanocrystals may occur. To explore the possibility of the energy transfer from the Ce³⁺ to Tb³⁺ ions, Tb³⁺ ions with different concentrations were doped into the BaY_{0.80}Ce_{0.20}F₅ nanocrystals. Figure 6 displays the excitation and emission spectra of the BaY_{0.80-x}Ce_{0.20}Tb_xF₅ nanocrystals. As shown in Figure 6a, the excitation spectrum BaY_{0.60}Ce_{0.20}Tb_{0.20}F₅ nanocrystals monitored at 543 nm consists mainly of the excitation bands of the Ce³⁺ ions and the weak absorption bands of the Tb³⁺ ions, revealing that the Tb³⁺ ions are essentially excited through the Ce³⁺ ions. In fact, several weak f–f absorption bands of the Tb³⁺ ions are just present in the region of the Ce³⁺ emission. Thus the energy transfer from the Ce³⁺ to Tb³⁺ ions occurs. The emission spectra of BaY_{0.80-x}Ce_{0.20}Tb_xF₅ nanocrystals (Figure 6b) contain both the weak emission of the Ce³⁺ ions and the strong green emission of the Tb³⁺ ions. The emission intensity of the Tb³⁺ ions gradually increases at the expense of that of the Ce³⁺ ions with the increase of Tb³⁺ doping concentration, indicating that the energy transfer from the Ce³⁺ to Tb³⁺ ions is highly efficient since the emission band of the Ce³⁺ ions matches well with the f–f absorptions of the Tb³⁺ ions. Moreover, it is worth noting that the BaY_{0.60}Ce_{0.20}Tb_{0.20}F₅ nanocrystals can be easily dispersed in hydrophilic solvents, such as water and ethanol. The pellucid dispersion of BaY_{0.60}Ce_{0.20}Tb_{0.20}F₅ colloidal nanocrystals in water under irradiation of a 254 nm UV lamp also exhibits bright green emission. The photographs shown in inset of Figure 6b demonstrate that these samples have great potential as biolabeling reagents in hydrophilic environment.

In order to investigate the luminescence dynamics of the samples, we measured the PL decay curves and then calculated the lifetime as well as energy transfer efficiencies. Figure 7 gives the PL decay curves of the Ce³⁺ ions in BaY_{0.80-x}Ce_{0.20}Tb_xF₅ nanoparticles which were excited at 290 nm and monitored at 330 nm. One can see that decay curve of the Ce³⁺ ions single-doped BaY_{0.80}Ce_{0.20}F₅ particles can be well fitted into a single-exponential function with a decay lifetime time of 40.61 ns. This is the radioactive decay time of the Ce³⁺ ions. For the

Ce³⁺ and Tb³⁺ ions codoped samples, the doping of Tb³⁺ ions significantly modifies the fluorescence dynamics of the Ce³⁺ ions. The results reveal that the fluorescence decays gradually deviate from a single-exponential rule, indicating the presence of a nonradiative process. The effective lifetime is defined as³⁶

$$\tau = \frac{\int_0^{\infty} tI(t)dt}{\int_0^{\infty} I(t)dt} \quad (1)$$

On the basis of eq 1, the effective lifetime values of the Ce³⁺ ions were calculated to be 30.94, 23.67, 18.84, 13.95, and 10.53 ns for BaY_{0.80-x}Ce_{0.20}Tb_xF₅ with $x = 0.04, 0.08, 0.12, 0.16$, and 0.20 , respectively. It can be seen that the decay lifetime of the Ce³⁺ ions decrease monotonically with increasing Tb³⁺ concentration, which strongly supports the energy transfer from the Ce³⁺ to Tb³⁺ ions.

The energy transfer efficiency (η_T) from the Ce³⁺ to Tb³⁺ ions in the BaY_{0.80-x}Ce_{0.20}Tb_xF₅ nanocrystals can be expressed by

$$\eta_T = 1 - \tau_s/\tau_{s0} \quad (2)$$

where τ_{s0} is the decay lifetime of the Ce³⁺ sensitizer and τ_s is the decay lifetime of the Ce³⁺ sensitizer in the presence of the Tb³⁺ ions. The energy transfer efficiency from the Ce³⁺ to Tb³⁺ ions in BaY_{0.80-x}Ce_{0.20}Tb_xF₅ nanoparticles were calculated and illustrated in Figure 8. The energy transfer efficiency η_T monotonically increased with increasing the Tb³⁺ doping concentrations.

According to the energy transfer theories of Dexter and Schulman, concentration quenching is due to the energy transfer from one activator to another in many cases until an energy sink in the lattice is reached.³⁷ As suggested by Blasse,³⁸ the average separation R_{Ce-Tb} can be expressed as follows:

$$R_{Ce-Tb} \approx 2 \left(\frac{3V}{4\pi C_{Ce} + Tb^N} \right)^{1/3} \quad (3)$$

where N is the number of sites that lanthanide ion can occupy in per unit cell, V is the volume of the unit cell, and C_{Ce+Tb} is the total doping concentration of the Ce³⁺ and Tb³⁺ ions. For

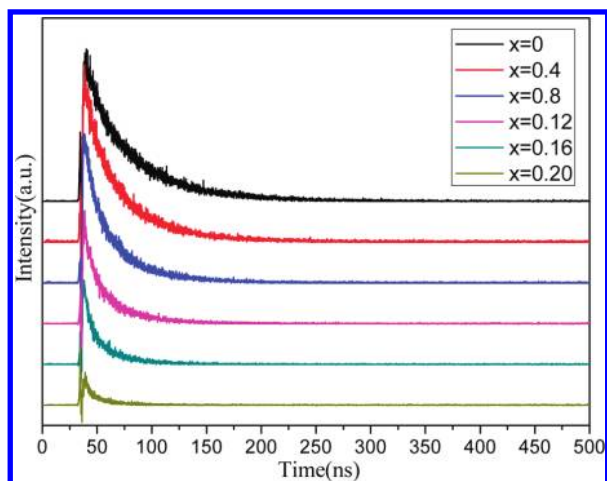


Figure 7. Emission decay curves of Ce³⁺ in the BaY_{0.80-x}Ce_{0.20}Tb_xF₅ nanocrystals (excited at 290 nm, monitored at 330 nm).

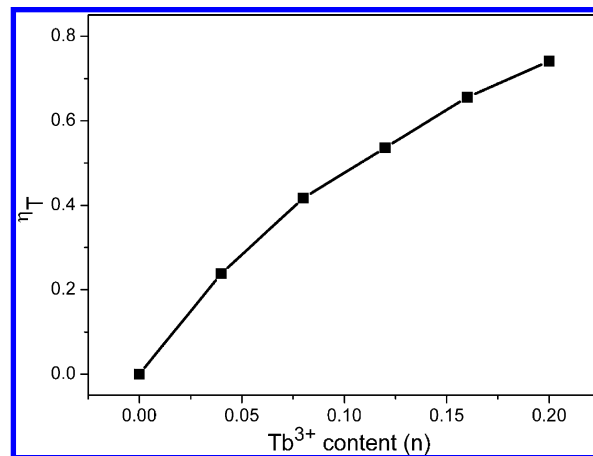


Figure 8. Dependence of the energy transfer efficiency η_T in BaY_{0.80-x}Ce_{0.20}Tb_xF₅ nanocrystals on the Tb³⁺ ions doping concentration.

the host of BaYF₅, $N = 2$, and $V = 204.360 \text{ \AA}^3$. Using formula 3, R_{Ce-Tb} (in \AA) is determined to be 9.92, 9.34, 8.87, 8.48, 8.16, and 7.87 \AA for $C_{Ce+Tb} = 0.20, 0.24, 0.28, 0.32, 0.36, 0.40$, respectively. The critical concentration C_{Ce+Tb} is defined as the concentration for which the emission intensity of the Ce³⁺ ions is half that of the sample in the absence of Tb³⁺ ions. In the host of the BaYF₅ nanocrystals, the critical concentration of C_{Ce+Tb} is 0.268 and the corresponding critical distance (R_c) for the Ce³⁺–Tb³⁺ energy transfer is about 9.00 \AA .

The energy transfer from a sensitizer to an activator may take place via radiative transfer, exchange interaction, and multipole–multipole interaction.³⁹ Generally speak, the existence of the radiative energy transfer from a sensitizer to an activator can be confirmed by the spectral dips in the emission spectrum of the sensitizer. This situation was observed in LaOBr containing Ce³⁺ and Ho³⁺ ions, where the Ce³⁺ emission band shows the dips corresponding to the f–f absorption lines of the Ho³⁺ ions and the origination of these dips were attributed to the radiative energy transfer from the Ce³⁺ to Ho³⁺ ions.⁴⁰ The absence of the dips in the emission band of the Tb³⁺ ions means that radiative energy transfer between the Ce³⁺ ions and the Tb³⁺ ions can be neglected. Moreover, the radiative energy transfer does not change the decay time of the sensitizer. The decrease of the decay time of the Ce³⁺ ions also does not support a radiative energy transfer process. Exchange interaction is strongly influenced by the distance between the sensitizer and activator and needs a large overlapping between sensitizer and activator orbitals. While both the Ce³⁺ and Tb³⁺ ions are reducing ions, such an exchange would require very high energy. Generally, the value of the critical distance is about $3\text{--}4 \text{ \AA}$ if the exchange is dominated.⁴¹ In our case, the critical distance of Ce³⁺ and Tb³⁺ is estimated to be 9.00 \AA , suggesting that energy transfer via exchange interaction can be excluded either. Thus we suspected that the energy transfer in BaY_{0.80-x}Ce_{0.20}Tb_xF₅ nanocrystals takes place via electric multipole–multipole interaction. On the basis of Dexter's energy transfer formula of multipolar interaction and Reisfeld's approximation, the following relation can be given as

$$\frac{\eta_0}{\eta} \propto C_{Ce+Tb}^{n/3} \quad (4)$$

where η_0 and η are the emission quantum efficiency of the Ce³⁺ ions in the absence and presence of the Tb³⁺ ions, respectively;

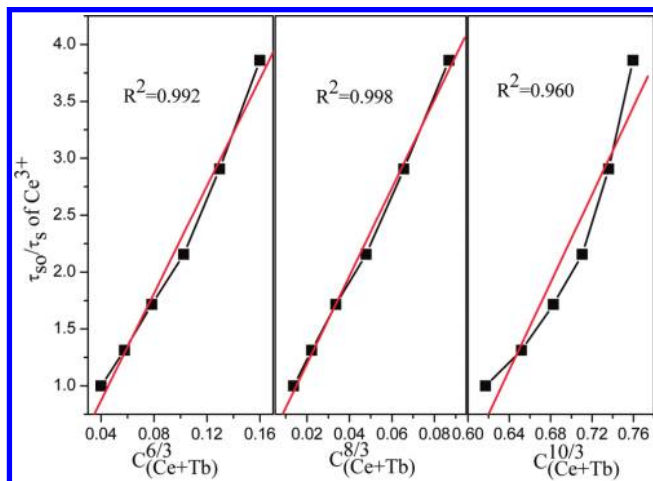


Figure 9. Dependence of τ_{so}/τ_s of Ce^{3+} on $C^{6/3}$, $C^{8/3}$ and $C^{10/3}$.

C_{Ce+Tb} is the total doping concentration of the Ce^{3+} and Tb^{3+} ions; and $n = 6, 8, 10$ corresponding to dipole–dipole, dipole–quadrupole, and quadrupole–quadrupole interactions, respectively. The value η_o/η can be approximately replaced by the ratio of related decay times (τ_{so}/τ_s). The $\tau_{so}/\tau_s - C^{n/3}$ plot (Figure 9) exhibits a good linear relation in dipole–quadrupole interaction, revealing that the dipole–quadrupole interaction should be mainly responsible for the energy transfer from the Ce^{3+} to Tb^{3+} ions.^{21,42}

According to Dexter's energy transfer theory,⁴³ the energy transfer process through multipolar interaction depends on the extent of overlap of the emission spectrum of the sensitizer with the absorption spectrum of the activator, the relative orientation of interacting dipoles and the distance between the sensitizer and the activator. For a dipole–dipole interaction, the energy transfer probability (P_{SA}) from a sensitizer to an activator is given by the following formula:

$$P_{SA}(dd) = \frac{3 \times 10^{12} f_d}{R^6 \tau_s} \int \frac{f_s(E) F_A(E)}{E^4} dE \quad (5)$$

where f_d is the oscillator strength of the involved dipole absorption transition of the activator, τ_s is the radiative decay time of the sensitizer, and R is the sensitizer–activator average distance, $f_s(E)$ represents the normalized emission shape function of the sensitizer and $F_A(E)$ the normalized absorption shape function of the activator, and E is the energy involved in the transfer (eV).

The critical distance (R_c) of the energy transfer from the sensitizer to activator is defined as the distance for which the probability of transfer equals the probability of radiative emission of the sensitizer, i.e. the distance for which $P_{SA} \cdot \tau_s = 1$. Therefore, R_c can be obtained from the formula (6):

$$R_c^6 = 3 \times 10^{12} f_d \int \frac{f_s(E) F_A(E)}{E^4} dE \quad (6)$$

The f_d of the Tb^{3+} transition is 0.3×10^{-6} .²¹ Using this value and the calculated spectral overlap, the critical distance for a dipole–dipole interaction mechanism is estimated to be 4.13 Å, which largely deviates from that estimated from the critical concentration data (9.00 Å), further indicating that the electric dipole–dipole interaction can be excluded as the main energy

transfer mechanism, which agree with the result obtained by Reisfeld's approximation. Dipole–dipole interactions can generally be expected to dominate in the energy-transfer when both the sensitizer and the activator ions are characterized by an electric dipole-allowed transition, while the $f-f$ transitions of the Tb^{3+} ion are forbidden by the selection rules of electric dipole transitions.⁴⁴

For dipole–quadrupole interaction, R_c can be expressed as follows:⁴⁵

$$R_c^8 = 3 \times 10^{12} \lambda_s^2 f_q \int \frac{f_s(E) F_A(E)}{E^4} dE \quad (7)$$

Where f_q is the oscillator strength of the involved quadrupole absorption transitions for the Tb^{3+} ions and λ_s (in Å) is the emission wavelength of the Ce^{3+} ions. The oscillator strength of the Tb^{3+} quadrupole transitions (f_q) did not obtained up to now. However, it is suggest by Versteegen et al. that the ratio f_q/f_d is about 10^{-2} – 10^{-3} when f_d applies to a forbidden dipole transition.²¹ Using $\lambda_s = 3300$ Å, $f_q = 10^{-2}$ – $10^{-3} f_d$, the critical distance is obtained to be 12.34–9.26 Å for the dipole–quadrupole interaction. Considering the critical distance (9.09 Å) obtained by formula (2), it allows us to conclude for the first time that the more reasonable ratio f_q/f_d for the Tb^{3+} ion is about 10^{-3} , which may be of much significance in the estimate of the critical distance of the dipole–quadrupole interaction between the Ce^{3+} and Tb^{3+} ions through the Dexter's energy transfer theory.

4. Conclusions

A simple and facile hydrothermal method was used to prepare BaYF₅ nanocrystals with a mean size of about 24 nm without any surfactant or chelator for the first time. By using a Rietveld refinement method with GSAS soft, we confirmed that the as-synthesized BaYF₅ nanocrystals were cubic structure crystals instead of the reported tetragonal structure. In the lattice of face-centered cubic structure BaYF₅, Ba^{2+} , and Y^{3+} ions occupy the same 4a Wyckoff position in half, while fluoride ions partially occupy four different Wyckoff positions of 4b, 8c, 32i, and 48f. A series of controlled experimental results demonstrated that BaYF₅ nanocrystals with similar size and morphology can be obtained in a variety of experimental conditions. The optical properties of the Eu^{3+} ions indicated that that the Eu^{3+} ions locate at the sites of inversion symmetry and further prove the rationality of the face-centered cubic structure of BaYF₅ host matrix. The emission spectra of the $BaY_{0.80-x}Ce_{0.20}Tb_xF_5$ nanocrystals with different Tb^{3+} concentrations demonstrated that the energy transfer from the Ce^{3+} to Tb^{3+} ions is highly efficient. By theoretical calculation and comparison, it inferred that the Ce^{3+} – Tb^{3+} energy transfer in BaYF₅: Ce^{3+} , Tb^{3+} nanocrystals occurs predominantly via the dipole–quadrupole interaction. The accurate ratio f_q/f_d for the Tb^{3+} ion was obtained, which may open a way to calculate the critical distance of the dipole–quadrupole interaction between the Ce^{3+} and Tb^{3+} ions in other luminescent materials. Furthermore, the BaYF₅ nanocrystals can be dispersed in water to form a pellucid solution and emit bright green emission, indicating that they are good candidates as biolabeling reagents.

Acknowledgment. This work is financially supported by the National Natural Science Foundation of China (Grant No. 20771098) and the NSFC Fund for Creative Research Group (Grant No. 20921002), and the National Basic Research Program of China (973 Program, Grant No. 2007CB935502).

Supporting Information Available: XRD patterns of different lanthanide ions doped BaYF₅ nanocrystals: (a) BaY_{0.95}-Eu_{0.05}F₅, (b) BaY_{0.80}Ce_{0.20}F₅, (c) BaY_{0.80}Tb_{0.20}F₅, (d) BaY_{0.60}Ce_{0.20}Tb_{0.20}F₅ (Figure S1); XRD pattern (a) and SEM image (b) of the YF₃ truncated octahedral microcrystals produced with pH 1 (Figure S2); SEM images of the BaYF₅ nanocrystals obtained with different amount of chelator EDTA: (a) 0.15 g, (b) 0.30 g, (c) 0.60 g (Figure S3); SEM images of the BaYF₅ nanocrystals obtained with different barium sources: (a) Ba(CH₃COO)₂, (b) Ba(NO₃)₂ (Figure S4); XRD patterns of the BaYF₅ nanocrystals obtained after different hydrothermal reaction time: (a) 0 h, (b) 1 h, (c) 6 h, (d) 12 h (Figure S5); The SEM images of the BaYF₅ nanocrystals obtained after different hydrothermal reaction time: (a) 0 h, (b) 1 h, (c) 6 h, and (d) 12 h (Figure S6). This material is available free of charge via the Internet at <http://pubs.acs.org>.

References and Notes

- Gill, R.; Zayats, M.; Willner, I. *Angew. Chem., Int. Ed.* **2008**, *47*, 7602.
- Wang, L. Y.; Yan, R. X.; Hao, Z. Y.; Wang, L.; Zeng, J. H.; Bao, H.; Wang, X.; Peng, Q.; Li, Y. D. *Angew. Chem. Int.* **2005**, *44*, 6054.
- Wang, M.; Mi, C. C.; Wang, W. X.; Liu, C. H.; Wu, Y. F.; Xu, Z. R.; Mao, C. B.; Xu, S. K. *ACS Nano* **2009**, *3*, 1580.
- (a) Liu, G. K.; Zhuang, H. Z.; Chen, X. Y. *J. Solid State Chem.* **2003**, *171*, 123–132. (b) Liu, G. K.; Zhuang, H. Z.; Chen, X. Y. *J. Nano Lett.* **2002**, *2*, 535.
- Jan, W. S.; Frank, V. *Langmuir* **2004**, *20*, 11763–11771.
- Di, W. H.; Wang, X. J.; Chen, B. J.; Lu, S. Z.; Zhao, X. X. *J. Phys. Chem. B* **2005**, *109*, 13154.
- Qiu, J. M.; Wang, J. P. *Adv. Mater.* **2007**, *19*, 1703.
- Bonil, K.; Reken, N. P.; Brian, A. K. *J. Am. Chem. Soc.* **2009**, *131*, 3134.
- Shankar, S. S.; Rai, A.; Ankamwar, B.; Singh, A.; Ahmad, A.; Sastry, M. *Nat. Mater.* **2004**, *3*, 482.
- Gao, P.; Xie, Y.; Li, Z. *Eur. J. Inorg. Chem.* **2006**, 3261.
- Hu, H.; Chen, Z. G.; Cao, T. Y.; Zhang, Q.; Yu, M. X.; Li, F. Y.; Yi, T.; Huang, C. H. *Nanotechnology* **2008**, *19*, 375702, (9pp).
- Zhuang, J. L.; Wang, J.; Yang, X. F.; Williams, I. D.; Zhang, W.; Zhang, Q. Y.; Feng, Z. M.; Yang, Z. M.; Liang, C. L.; Wu, M. M.; Su, Q. *Chem. Mater.* **2009**, *21*, 160.
- Zhang, F.; Li, J.; Shan, J.; Xu, L.; Zhao, D. Y. *Chem.—Eur. J.* **2009**, *15*, 11010.
- Huang, Y. J.; You, H. P.; Jia, G.; Zheng, Y. H.; Song, Y. H.; Yang, M.; Liu, K.; Zhang, L. H. *J. Phys. Chem. C* **2009**, *113*, 16962.
- Liu, X. R.; Xu, G.; Richard, C. P. *J. Solid State Chem.* **1986**, *62*, 83.
- Guggenheim, H. J.; Johnson, L. F.; Hill, M. *Appl. Phys. Lett.* **1969**, *15*, 51.
- Yi, G. S.; Lee, W. B.; Chow, G. M. *J. Nanosci. Nanotechnol.* **2007**, *7*, 2790.
- Vetrone, F.; Mahalingam, V.; Capobianco, J. A. *Chem. Mater.* **2009**, *21*, 1847.
- Chiu, Y. C.; Liu, W. R.; Yeh, Y. T.; Jang, S. M.; Chen, T. M. *J. Electrochem. Soc.* **2009**, *156*, J221.
- Jüstel, T.; Nikol, H.; Ronda, C. *Angew. Chem., Int. Ed.* **1998**, *37*, 3084.
- Vestegen, J. M. P. J.; Sommerdijk, J. L.; Verriet, J. G. *J. Lumin.* **1973**, *6*, 425.
- You, H. P.; Wu, X. Y.; Hong, G. Y.; Tang, J. K.; Hu, H. P. *Chem. Mater.* **2003**, *15*, 2000.
- Rietveld, H. M. *J. Appl. Crystallogr.* **1969**, *2*, 65.
- Larson, A. C.; Von Dreele, R. B. *General Structure Analysis System Technical Manual LANSCE, MS-H805*; Los Alamos National University LAUR: Los Alamos, 2000; p 86.
- Yong, K. T.; Swihart, M. T.; Ding, H.; Prasad, P. N. *Plasmonics* **2009**, *4*, 79.
- Li, J.; Zeng, H. C. *J. Am. Chem. Soc.* **2007**, *129*, 15839.
- Liang, X.; Xu, B.; Kuang, S. M.; Wang, X. *Adv. Mater.* **2008**, *20*, 3739.
- Wckoever, S. W. S.; Brown, M. D.; Abbundi, T. J.; Chan, H.; Mathur, V. K. *J. Appl. Phys.* **1986**, *60*, 2505.
- U aldiño, G. *J. Phys.: Condens. Matter* **2003**, *15*, 7127.
- Tao, F.; Wang, Z. J.; Yao, L. Z.; Cai, W. L.; Li, X. G. *J. Phys. Chem. C* **2007**, *111*, 3241.
- Chen, X. Y.; Liu, G. K. *J. Solid State Chem.* **2005**, *178*, 419.
- Lai, H.; Bao, A.; Yang, Y. M.; Tao, Y. C.; Yang, H.; Zhang, Y.; Han, L. L. *J. Phys. Chem. C* **2008**, *112*, 282.
- Yang, M.; You, H. P.; Song, Y. H.; Huang, Y. J.; Jia, G.; Liu, K.; Zheng, Y. H.; Zhang, L. H.; Zhang, H. J. *J. Phys. Chem. C* **2009**, *113*, 20173.
- Zhang, Q. H.; Wang, J.; Zhang, G. G.; Su, Q. *J. Mater. Chem.* **2009**, *19*, 7088.
- Hirai, T.; Kondo, Y. *J. Phys. Chem. C* **2007**, *111*, 168.
- Liu, K.; You, H. P.; Zheng, Y. H.; Jia, G.; Song, Y. H.; Huang, Y. J.; Yang, M.; Jia, J. J.; Guo, N.; Zhang, H. J. *J. Mater. Chem.* **2010**, *20*, 3272.
- Dexter, D. L.; Schulman, J. A. *J. Chem. Phys.* **1954**, *22*, 1063.
- Blasse, G. *Philips. Res. Rep.* **1969**, *24*, 131.
- Liu, G. K.; Jacquier, B. *Spectroscopic Properties of Rare Earths in Optical Materials*; Springer: Beijing, 2005.
- Youmo, L.; Guillen, F.; Fouassier, C.; Hagenmuller, P. *J. Electrochem. Soc.* **1985**, *132*, 717–721.
- Antipeuko, B. M.; Bataev, I. M.; Ermolaev, V. L.; Lyubimov, E. I.; Privalova, T. A. *Opt. Spectrosc.* **1970**, *29*, 177.
- U aldiño, G. *J. Phys.: Condens. Matter* **2003**, *15*, 3821.
- Dexter, D. L. *J. Chem. Phys.* **1953**, *21*, 836.
- Zhang, Z.; Wang, J.; Zhang, M.; Zhang, Q.; Su, Q. *Appl. Phys. B: Laser Opt.* **2008**, *91*, 529.
- You, H. P.; Zhang, J. L.; Hong, G. Y.; Zhang, H. J. *J. Phys. Chem. C* **2007**, *111*, 10657.

JP105061X